Journal of the Optical Society of America A
OPTICS, IMAGE SCIENCE, AND VISION

Anti-resonant fiber with high-resistivity silicon for THz wave transmission

Qiang Liu,[1,2] Guangrong Sun,[1,2] Yudan Sun,[3] Wei Liu,[1,2] Chao Ma,[1,2] Wenjing Li,[1,2] Kaiyu Wang,[1,2] Jingwei Lv,[1,2] Paul K. Chu,[4] and Chao Liu[1,2,*]

[1]School of Physics and Electronic Engineering, Northeast Petroleum University, Daqing 163318, China
[2]SANYA Offshore Oil & Gas Research Institute, Northeast Petroleum University, Sanya 572024, China
[3]College of Mechanical and Electrical Engineering, Daqing Normal University, Daqing 163712, China
[4]Department of Physics, Department of Materials Science and Engineering, and Department of Biomedical Engineering, City University of Hong Kong, Tat Chee Avenue, Kowloon, Hong Kong, China
*msm-liu@126.com

Received 15 June 2023; revised 8 October 2023; accepted 18 October 2023; posted 18 October 2023; published 1 November 2023

A novel anti-resonant fiber for low-loss terahertz waveguides is proposed and analyzed. The terahertz fiber uses high-resistivity silicon as the bulk material and nine nested double-layer concentric circular tubes in the cladding to reduce propagation losses. The effects of the geometric parameters on the propagation characteristics are analyzed by the finite element method. The result indicates that an ultra-low total loss of 4.9×10^{-4} dB/m is achieved at $f = 1$ THz. The low-loss propagation window is 0.48 THz ranging from 0.6 to 1.4 THz. In addition, the influence of mechanical bending on the propagation loss is investigated and the bending loss can be maintained at less than 7.3×10^{-3} dB/m at $f = 1$ THz even if the bending radius is larger than 60 cm. The properties of this anti-resonant fiber are significantly superior to those of previously reported structures and the fiber thus has large commercial potential.

https://doi.org/10.1364/JOSAA.498066

1. INTRODUCTION

As a kind of special fiber, hollow-core fibers (HCFs) have the advantages of low nonlinearity, low dispersion, low material absorption loss, high damage thresholds, and low propagation latency [1] as well as some applications in high power delivery [2], high-speed data communication [3], ultra-short pulse delivery [4], pulse compression [5], supercontinuum [6], gas fiber lasers [7], and gas nonlinear optics [8]. HCFs mainly include photonic bandgap fibers [9] (PBGFs) and anti-resonant fibers [10] (ARFs). The PBGFs utilize periodically arranged air holes in the cladding to confine the light in the core, and the propagation loss can be reduced by adjusting the cladding structure. However, the propagation windows of PBGFs are usually relatively limited, whereas ARFs can overcome the window limitation and exhibit favorable propagation properties, including small nonlinearity, low propagation loss, and controllable dispersion [11].

The ARFs are on the basis of the "Fano resonance" mechanism which prevents the coupling between the core mode and cladding modes to realize light propagation in various spectral bands. Owing to the particularity of the terahertz (THz) regime, the propagation losses of reported THz ARFs are relatively high. Setti *et al*. fabricated a THz ARF consisting of six single-layer circular tubes constructed with PMMA [12] and observed a total loss of 16 dB/m at $f = 0.828$ THz. Hasanuzzaman *et al*. designed a THz ARF composed of six nested circular tubes based on Topas [13]. The confinement loss (CL) is only 3.4307×10^{-4} dB/m, but the total loss reaches 0.05 dB/m at $f = 1$ THz due to the larger effective material loss. The low-loss propagation window is 0.4 THz. Mollah *et al*. simulated a THz ARF with six half circular tubes and half elliptical tubes using Zeonex [14]. The confinement loss of the order of 10^{-4} dB/m and the effective material loss (EML) of 0.034 dB/m can be achieved at $f = 1$ THz. The total loss of the fiber is 0.034 dB/m, which is mainly determined by the effective material loss, and the low-loss propagation window is 0.5 THz. Sultana *et al*. numerically analyzed three THz ARFs composed of nonnested circular tubes, nested circular tubes, and adjacent nested circular tubes based on Zeonex [15]. The results show that the THz ARF with five nested circular tubes has a relatively low total loss of 0.055 dB/m at $f = 1$ THz. Comparison of these results reveals that the effective material losses of these above-mentioned THz ARFs are still not mitigated inadequately. Therefore, we proposed a THz ARF using six nested double-layer U-shape tubes in conjunction with high-resistivity silicon (HRS) [16]. The refractive index is considered as a constant of 3.417 in the 0.5–4.5 THz range and the bulk material absorption loss is less than 1.5 m^{-1} in the range of 0.1–1.5 THz [17], which is much less than that of 27.6 m^{-1} and 20 m^{-1} for Topas [13] and Zeonex [14] around 1 THz.

The HRS has been used in designing photonic crystal fibers in the terahertz regime [18–20]. The optimized fiber shows an effective material loss of 5×10^{-4} dB/m and a confinement loss of 2.6×10^{-3} dB/m, achieving a total loss of 3.1×10^{-3} dB/m at $f = 1$ THz and a low-loss propagation window of 0.44 THz. However, it is difficult to further reduce the confinement loss due to the ultra-high refractive index of HRS.

Herein, a THz ARF based on HRS with nine nested double-layer concentric circular tubes is designed and analyzed. This structure reduces the confinement loss to 2.6×10^{-4} dB/m. The effective material loss is only 2.3×10^{-4} dB/m and the total loss reaches 10^{-4} dB/m for the first time in the frequency ranges of 0.88–0.92 THz and 0.96–1.14 THz. Moreover, the ARF exhibits good bending resistance, as manifested by a bending loss of less than 7.3×10^{-3} dB/m at $f = 1$ THz in spite of the bending radius being larger than 60 cm.

2. GEOMETRY OF THE PROPOSED FIBER

The cross section of the proposed ARF structure is illustrated in Fig. 1. The core diameter is $D_c = 6.2$ mm, and the external and internal layer diameters are $d_1 = 2.4$ mm and $d_2 = 1.5$ mm, respectively. A large core diameter will result in a high bending loss due to the large mode field area. Therefore, our proposed fiber uses a nine-tube structure to suppress bending loss caused by the large core diameter. The cladding consists of nine nested double-layer concentric circular tubes connected by solid supporting rods. This structure can better maintain the concentricity and stability of the ARF, avoiding fiber deformation. The uniform anti-resonant wall thickness of the cladding structure is $t = 0.035$ mm. The thicknesses of the jacket tube and perfectly matched layer are $JT = 0.15$ mm and $T = 0.5$ mm, respectively, and the internal radius of the ARF is $R_i = 5.5$ mm. In order to ensure accurate numerical calculations, extremely fine mesh sizes of $\lambda/6$ and $\lambda/4$ are adopted in the HRS and air parts, respectively [21,22].

3. ANALYSIS AND DISCUSSION

According to the principle of the anti-resonant reflecting optical waveguide, light propagation in the core will generate higher losses at the resonant frequencies and hence, it is essential to avoid the resonant frequency to obtain a lower propagation loss and wider propagation window, which can be calculated by Eq. (1) [23–26]:

$$f_c = \frac{mc}{2t\sqrt{n^2 - 1}}, \tag{1}$$

where c represents the velocity of light in vacuum, m represents the order of resonance, n represents the refractive index of the bulk material, and t represents the wall thickness.

The confinement loss (CL) and effective material loss (EML) of the THz ARF can be shown by Eqs. (2) and (3) [27–30]:

$$\mathrm{CL} = 8.686 \left(\frac{2\pi f}{c}\right) \mathrm{Im}\,(n_{\mathrm{eff}})\,, \ \left[\mathrm{dB/m}\right], \tag{2}$$

$$\mathrm{EML} = 4.34\sqrt{\frac{\varepsilon_0}{\mu_0}} \frac{\int_{A_{\mathrm{mat}}} n\alpha_{\mathrm{mat}} |E|^2 \mathrm{d}A}{2\int_{\mathrm{All}} S_z \mathrm{d}A}, \ [\mathrm{dB/m}], \tag{3}$$

where f is the operating frequency; $\mathrm{Im}(n_{\mathrm{eff}})$ is the imaginary part of the effective refractive index; ε_0 and μ_0 are the permittivity and permeability in vacuum, respectively; α_{mat} is the bulk material absorption loss; and S_z is the Poynting vector along the propagation direction of z, which is defined as $S_z = \frac{1}{2}\mathrm{Re}(E \times H^*)z$, where E is the electric field and H is the magnetic field.

The influence of the wall thickness t of the nested concentric circular tubes on the propagation loss properties is analyzed. For $R_i = 5.5$ mm, $JT = 0.15$ mm, $D_c = 6.2$ mm, $d_1 = 2.4$ mm, and $d_2 = 1.5$ mm, the spectra in Fig. 2(a) present the CL for various wall thicknesses. The low-loss band of the CL spectra ($<10^{-1}$ dB/m) is narrowest, and the smallest CL is 1.4×10^{-3} dB/m as $t = 0.05$ mm. With decreasing the wall thickness, the CL spectra shift to higher frequency direction.

The CL decreases progressively, and the low-loss band broadens. The reason for this phenomenon is that a thinner wall produces a higher resonant frequency according to Eq. (1), and the low-loss band is broader. Meanwhile the nested double-layer tubes result in numerous oscillation peaks due to the intense couplings between the external and internal layer concentric circular tubes [31]. The low-loss band of the CL spectra is broadest, and the lowest CL is 2.5×10^{-4} dB/m as $t = 0.035$ mm. The spectra in Fig. 2(b) exhibit EMLs for various wall thicknesses. As the wall thickness decreases, the EML spectra exhibit a similar trend as the CL spectra. The lowest EML is 2.3×10^{-4} dB/m.

The total loss (TL) spectra for various wall thicknesses can be obtained by superposing the CL and EML spectra, as shown in Fig. 3. With decreasing the wall thickness, the lowest TL decreases progressively. For $t = 0.035$ mm, the lowest TL is only 4.8×10^{-4} dB/m. The low-loss window ($<10^{-1}$ dB/m) also increases as the wall thickness decreases. As $t = 0.035$ mm, the low-loss propagation window is 0.48 THz, and the frequency being less than 10^{-3} dB/m is 0.22 THz. Hence, our ARF reduces the propagation loss and achieves a wide window and low-loss propagation at the same time.

For $R_i = 5.5$ mm, $JT = 0.15$ mm, $d_2 = 1.5$ mm, and $t = 0.035$ mm, the impact of the external layer diameter d_1 of the nested concentric circular tubes on the propagation loss properties is illustrated in Fig. 4(a). When $d_1 = 2$ mm, the low-loss window of the ARF is narrowest. As the external

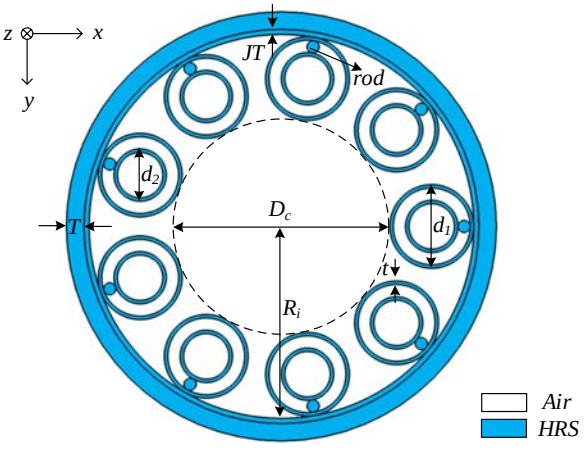

Fig. 1. Cross section of the ARF.

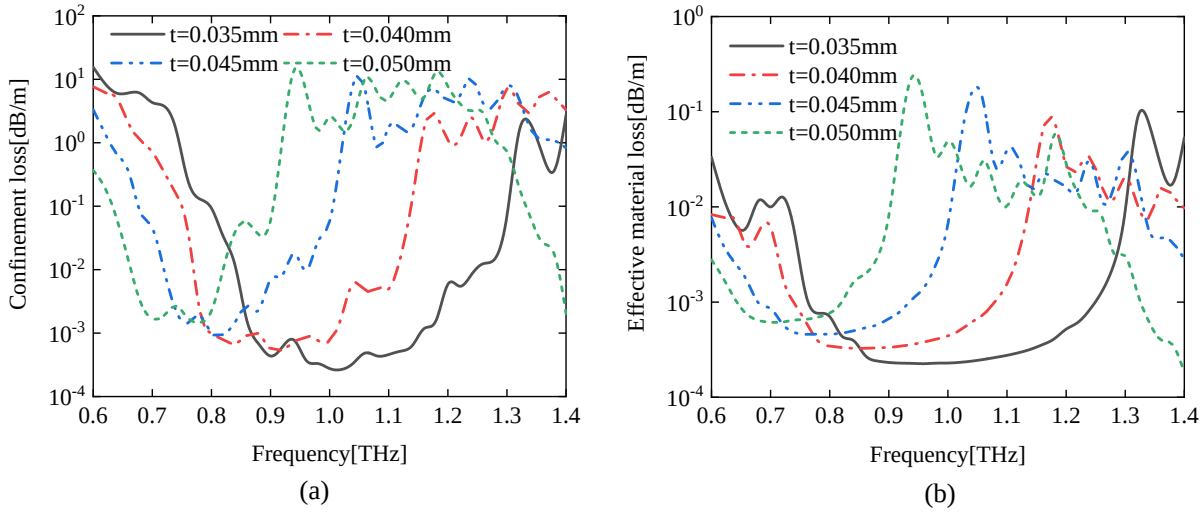

Fig. 2. (a) CL and (b) EML versus frequencies for various wall thicknesses.

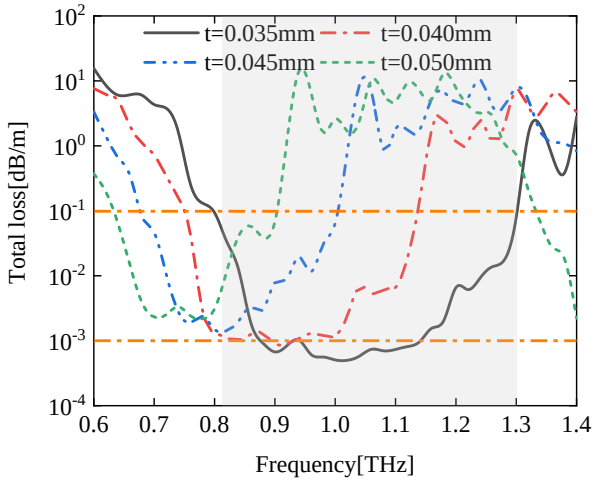

Fig. 3. TL versus frequencies for various wall thicknesses.

layer diameter goes up, the difference of the TL spectra for $d_1 = 2.2$ mm, 2.4 mm, and 2.6 mm is smaller. In order to determine the optimal d_1, the CL, EML, and TL for various external layer diameters at $f = 1$ THz are derived as manifested in Fig. 4(b). Compared to the CL, the EML exhibits a smaller effect as shown by the solid red curve. The solid blue curve presents the TL, and the insets show the contour plots of the mode fields for various external layer diameters. The TL decreases as the external layer diameter increases initially and then increases slowly. It is because when the external layer diameter is relatively small, the distance between adjacent tubes is large and it is easier for the mode field to leak through the gap to produce greater losses, as shown in the inset signed by the red border curve. As the external layer diameter goes up, the mode field is restricted in the core as presented in the contour plots of the mode field (purple and green border curves). As the external layer diameter continues to increase, the loss increases slightly due to additional resonance between adjacent tubes [32].

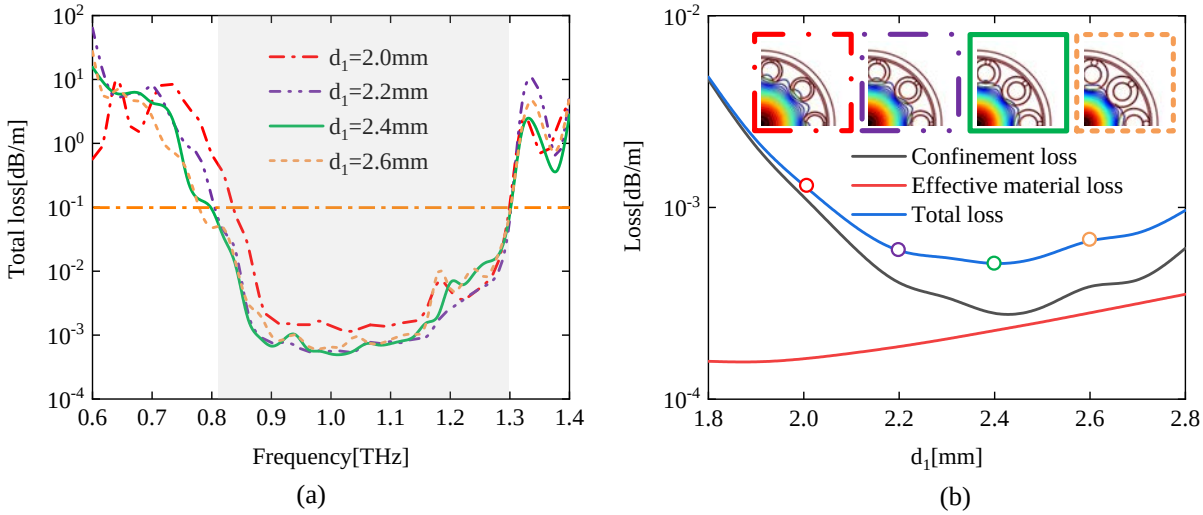

Fig. 4. (a) TL versus frequencies for various external layer diameters and (b) loss versus external layer diameters at $f = 1$ THz.

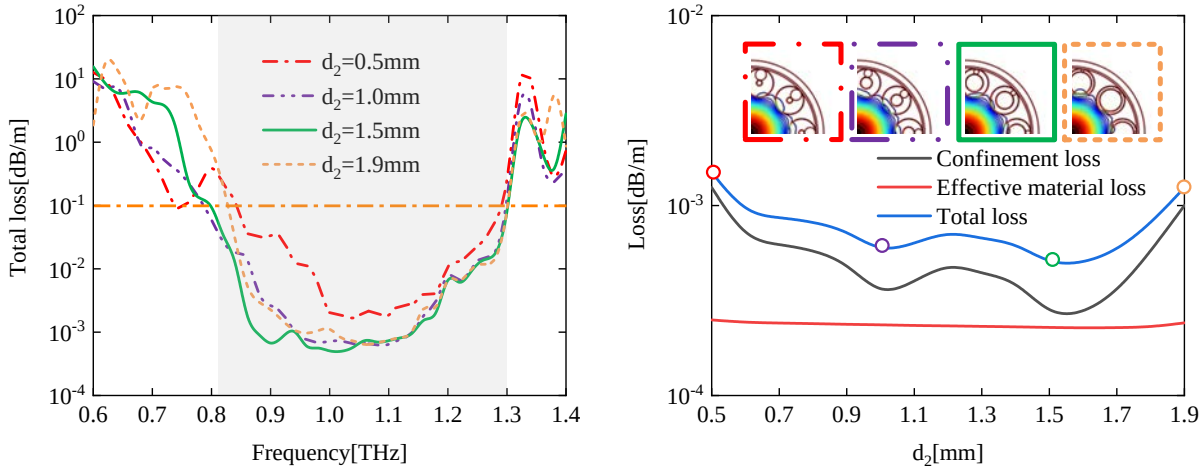

Fig. 5. (a) TL versus frequencies for various internal layer diameters and (b) loss versus internal layer diameters at $f = 1$ THz.

Therefore, $d_1 = 2.4$ mm shows the smallest TL and is selected to be the preferred value.

The impact of the internal layer diameter d_2 of the nested concentric circular tubes on the propagation loss properties is derived and displayed in Fig. 5(a). When the internal layer diameter is relatively small ($d_2 = 0.5$ mm), the lowest loss is slightly higher, and the value is 1.4×10^{-3} dB/m. As the internal layer diameter goes up, the TL spectra show smaller differences for $d_2 = 1.0$ mm, 1.5 mm, and 1.9 mm. This is because the double-layer anti-resonant effect can better restrict the mode field in the core [33]. To determine the optimal d_2, the CL, EML, and TL for various internal layer diameters at $f = 1$ THz are derived and displayed in Fig. 5(b). The internal layer diameter hardly influences the EML, but has a significant impact on the CL. The solid blue curve represents the TL, and the insets display the contour plots of the mode fields for various internal layer diameters. The mode field is limited in the core for $d_2 = 1.5$ mm, which corresponds to the lowest TL and is selected to be the preferred value.

The effect of the quantity of the nested concentric circular tubes on the propagation loss properties is investigated. As for $R_i = 5.5$ mm, $JT = 0.15$ mm, $D_c = 6.2$ mm, $d_1 = 2.4$ mm, $d_2 = 1.5$ mm, and $t = 0.035$ mm, the TL spectra and the contour plots of the mode field for various quantities of tubes are shown in Fig. 6. As the quantity of the nested concentric circular tubes is six, the mode field is not limited in the core due to the larger distance between adjacent tubes revealed by the contour plots of the mode field (red frame) at $f = 1$ THz. The smallest TL is 1.3×10^{-2} dB/m. As the amount of the nested concentric circular tubes is seven, the distance between adjacent tubes decreases resulting in smaller mode field leakage, as shown in the purple inset. The smallest value in the TL spectra is 1.6×10^{-3} dB/m. As the numbers of the nested concentric circular tubes are eight and nine, the TL spectra show almost the same trend. The insets marked by the green and orange frames are also consistent, indicating that the mode field is limited in the core. It means that more tubes can avoid mode field leakage through the gap of the adjacent tubes for large core ARF and the TL can be controlled.

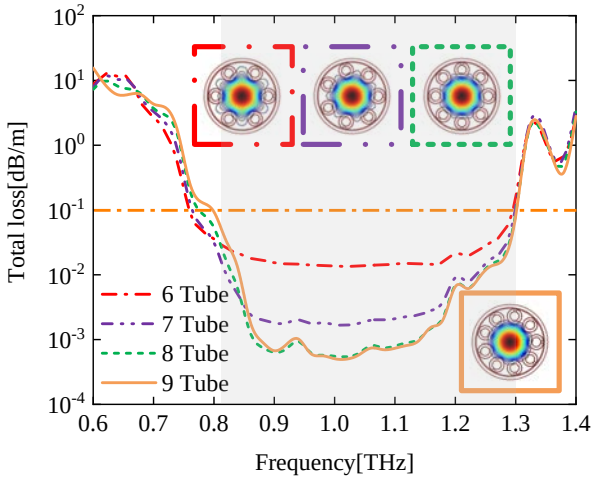

Fig. 6. TL versus frequencies for various quantities of tubes.

In order to further compare and optimize the eight-tube and nine-tube structures, the bending characteristic of the THz ARF is analyzed. By the conformal transformation method, we use an equivalent refractive index n_{eq} to compute bending loss expressed by Eq. (4) [34,35]:

$$n_{eq} = n \exp[x \cos\theta + y \sin\theta / R_b], \tag{4}$$

where n denotes the refractive index distribution of straight fiber cross section, R_b denotes the bending radius, and θ denotes the bending angle referred to an angle between the bending axis and positive x axis. The bending loss can be calculated by taking the n_{eq} into Eq. (2).

As the bending angle θ is 0° (along the x direction) and 180° (along the $-x$ direction), the bending losses of the eight-tube and nine-tube structures for various bending radii at $f = 1$ THz are depicted in Figs. 7(a) and 7(c). The bending loss of the nine-tube structure is lower demonstrating good bending resistance. Therefore, the nine-tube cladding is selected as the optimal structure and the bending characteristics are further analyzed. When the ARF is bent, the mode field in the core

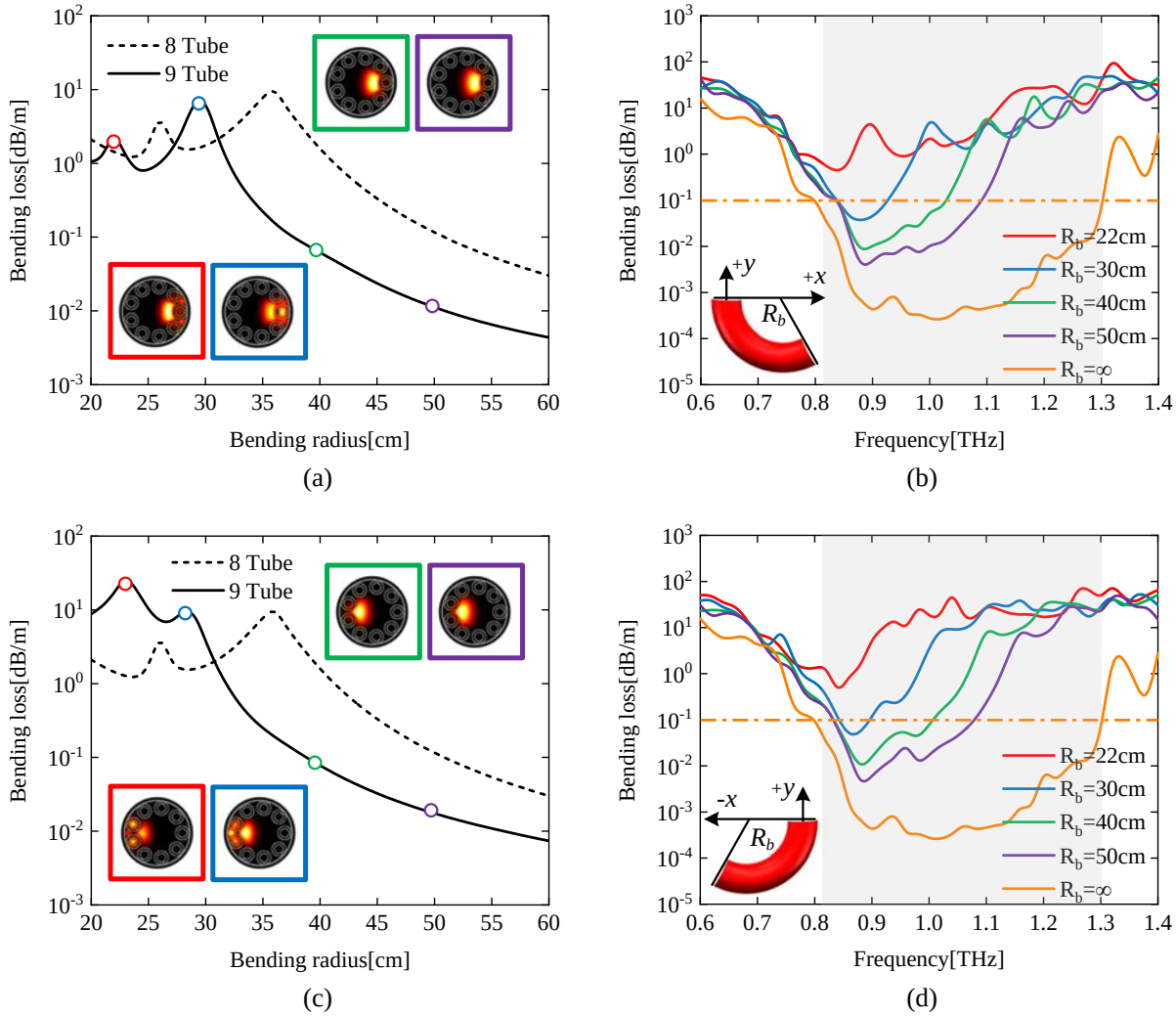

Fig. 7. (a) Bending losses at a bending angle $\theta = 0°$ versus radii at $f = 1$ THz, (b) bending losses at a bending angle $\theta = 0°$ versus frequencies for various bending radii, (c) bending losses at a bending angle $\theta = 180°$ versus radii at $f = 1$ THz, and (d) bending losses at a bending angle $\theta = 180°$ versus frequencies for various bending radii.

deviates radially toward the bending direction. The mode field is still concentrated in the core for a larger bending radius presented in the green and purple insets of Figs. 7(a) and 7(c). However, the bending loss goes up progressively with going down bending radius and higher loss peaks occur. The red and blue insets show that the mode fields in the core partially leak to the cladding. The loss peaks due to resonances between the core mode and cladding modes appear when the phases of the modes match [12].

Figures 7(b) and 7(d) show the bending loss spectra for bending angles of $\theta = 0°$ and 180° for various bending radii. When $R_b = 22$ cm, the bending loss spectrum has no low-loss band. The phenomenon mainly stems from the fact that bending disrupts the central symmetric structure of straight fiber and distorts the refractive index distribution to increase the bending loss [15]. When $R_b = 30$ cm, the bending loss decreases, and the low-loss band appears. A larger bending radius leads to a wider low-loss band. When the bending radius approaches infinity, the low-loss window is the widest and the loss is the lowest. Table 1 compares the propagation characteristics between our ARF and previously reported ARFs. It can be observed that our large core ARF reduces the EML and suppresses the CL giving rise to an ultra-low TL of 10^{-4} dB/m. The performance is better than the previous small core ARF [16]. The proposed fiber shows improved propagation characteristic as a terahertz waveguide. The flexibility and bendability of this fiber can be improved by adding a coating layer.

4. CONCLUSION

An ARF consisting of nine nested double-layer concentric circular tubes is presented and investigated. The HRS decreases the EML in the terahertz spectral range and the ARF structure suppresses the CL. The CL and EML are as low as 2.6×10^{-4} dB/m and 2.3×10^{-4} dB/m at $f = 1$ THz, respectively. The TL reaches the order of 10^{-4} dB/m for the first time, and the low-loss propagation window is 0.48 THz. At the same time, the ARF exhibits good bending resistance. As the bending radius is larger than 60 cm, the bending loss at

Table 1. Comparison between Our ARF and Previously Reported ARFs

Reference	Material Type	CL (dB/m)	EML (dB/m)	TL (dB/m)	Propagation Window (THz)	Operating Frequency (THz)
Ref. [36]	PMMA	8	/	/	/	2.52
Ref. [37]	HDPE	7	/	/	/	2.52
Ref. [12]	PMMA	/	/	16	/	0.828
Ref. [13]	Topas	3.4307×10^{-4}	0.05	0.05	0.4	1.0
Ref. [38]	Topas	3.2×10^{-4}	/	/	/	2.44
Ref. [14]	Zeonex	$\sim 10^{-4}$	0.034	0.034	0.5	1.0
Ref. [15]	Zeonex	/	0.055	0.055	/	1.0
Ref. [16]	HRS	2.6×10^{-3}	5×10^{-4}	3.1×10^{-3}	0.44	1.0
This work	HRS	2.6×10^{-4}	2.3×10^{-4}	4.9×10^{-4}	0.48	1.0

$f = 1$ THz is less than 7.3×10^{-3} dB/m. The excellent performance of the ARF suggests enormous application potential for terahertz waveguides.

Funding. City University of Hong Kong Donation Research Grant (DON-RMG 9229021); City University of Hong Kong Strategic Research Grant (SRG) (7005505); China Postdoctoral Science Foundation funded project (2020M670881); Natural Science Foundation of Heilongjiang Province (LH2021F007); Local Universities Reformation and Development Personnel Training Supporting Project from Central Authorities; Youth Science Foundation of Northeast Petroleum University (2019QNL-17); Hainan Province Science and Technology Special Fund (ZDYF2022GXJS003).

Disclosures. The authors declare no conflicts of interest.

Data availability. Data underlying the results presented in this paper are not publicly available at this time but may be obtained from the authors upon reasonable request.

REFERENCES

1. D. Wu, F. Yu, Y. Liu, and M. Liao, "Dependence of waveguide properties of anti-resonant hollow-core fiber on refractive index of cladding material," J. Lightwave Technol. **37**, 5593–5599 (2019).
2. G. Humbert, J. C. Knight, G. Bouwmans, P. S. J. Russell, D. P. Williams, P. J. Roberts, and B. J. Mangan, "Hollow core photonic crystal fibers for beam delivery," Opt. Express **12**, 1477–1484 (2004).
3. S. Gao, Y. Wang, W. Ding, D. Jiang, S. Gu, X. Zhang, and P. Wang, "Hollow-core conjoined-tube negative-curvature fibre with ultralow loss," Nat. Commun. **9**, 2828 (2018).
4. B. Debord, A. Amsanpally, M. Chafer, A. Bas, M. Maurel, J. M. Blondy, E. Hugonnot, F. Scol, L. Vincetti, F. Gerome, and F. Benabid, "Ultralow transmission loss in inhibited-coupling guiding hollow fibers," Optica **4**, 209–217 (2017).
5. F. Gerome, K. Cook, A. K. George, W. J. Wadsworth, and J. C. Knight, "Delivery of sub-100 fs pulses through 8 m of hollow-core fiber using soliton compression," Opt. Express **15**, 7126–7131 (2007).
6. F. Belli, A. Abdolvand, W. Chang, J. C. Travers, and P. S. J. Russell, "Vacuum-ultraviolet to infrared supercontinuum in hydrogen-filled photonic crystal fiber," Optica **2**, 292–300 (2015).
7. M. Xu, F. Yu, M. R. A. Hassan, and J. C. Knight, "Continuous-wave mid-infrared gas fiber lasers," IEEE J. Sel. Top. Quantum Electron. **24**, 0902308 (2018).
8. P. S. J. Russell, P. Holzer, W. Chang, A. Abdolvand, and J. C. Travers, "Hollow-core photonic crystal fibres for gas-based nonlinear optics," Nat. Photonics **8**, 278–286 (2014).
9. L. Vincetti, "Hollow core photonic band gap fiber for THz applications," Microw. Opt. Technol. Lett. **51**, 1711–1714 (2009).
10. F. Poletti, "Nested antiresonant nodeless hollow core fiber," Opt. Express **22**, 23807–23828 (2014).
11. A. Mollah, S. Rana, and H. Subbaraman, "Polarization filter realization using low-loss hollow-core anti-resonant fiber in THz regime," Results Phys. **17**, 103092 (2020).
12. V. Setti, L. Vincetti, and A. Argyros, "Flexible tube lattice fibers for terahertz applications," Opt. Express **21**, 3388–3399 (2013).
13. G. K. M. Hasanuzzaman, S. Iezekie, C. Markos, and S. Habib, "Hollow-core fiber with nested anti-resonant tubes for low-loss THz guidance," Opt. Commun. **426**, 477–482 (2018).
14. A. Mollah, S. Habib, and S. Habib, "Novel hollow-core asymmetric conjoined-tube anti-resonant fiber for low-loss THz wave guidance," OSA Contin. **3**, 1169–1176 (2020).
15. J. Sultana, S. Islam, C. M. B. Cordeiro, S. Habib, A. Dinovitser, B. W. Ng, and D. Abbott, "Exploring low loss and single mode in antiresonant tube lattice terahertz fibers," IEEE Access **8**, 113309 (2020).
16. G. Sun, Q. Liu, H. Mu, Y. Sun, S. Wang, M. Han, J. Wang, J. Lv, P. K. Chu, and C. Liu, "Anti-resonant fiber with nested U-shape tubes for low-loss terahertz waveguides," Opt. Laser Technol. **163**, 109424 (2023).
17. J. Dai, J. Zhang, W. Zhang, W. Zhang, and D. Grischkowsky, "Terahertz time-domain spectroscopy characterization of the far-infrared absorption and index of refraction of high-resistivity, float-zone silicon," J. Opt. Soc. Am. B **21**, 1379–1386 (2004).
18. T. Yang, C. Ding, R. W. Ziolkowski, and Y. J. Guo, "A scalable THz photonic crystal fiber with partially-slotted core that exhibits improved birefringence and reduced Loss," J. Lightwave Technol. **36**, 3408–3417 (2018).
19. B. Wang, F. Tian, G. Liu, C. Yao, L. Li, X. Yang, and J. Zhang, "A modified single-polarization THz fiber with epsilon-near-zero (ENZ) material," Results Opt. **1**, 100034 (2020).
20. T. Yang, C. Ding, R. W. Ziolkowski, and Y. J. Guo, "Circular hole ENZ photonic crystal fibers exhibit high birefringence," Opt. Express **26**, 17264–17278 (2018).
21. S. Habib, A. I. Adamu, C. Markos, and R. A. Correa, "Enhanced birefringence in conventional and hybrid anti-resonant hollow-core fibers," Opt. Express **29**, 12516–12530 (2021).
22. S. Habib, J. E. A. Lopez, C. Markos, A. Schulzgen, and R. A. Correa, "Single-mode, low loss hollow-core anti-resonant fiber designs," Opt. Express **27**, 3824–3836 (2019).
23. Z. Han, F. Tian, Y. Lu, G. Hu, Y. Chen, Z. Zeng, C. Liu, X. Yang, L. Li, and J. Zhang, "A single-polarization hollow-core anti-resonant fiber based on epsilon-near-zero (ENZ) material in terahertz region," Optik **279**, 170598 (2023).
24. S. Liu, L. Zhang, M. Tian, T. Yang, and Y. Dong, "Epsilon negative-based, broadband single-polarization single-mode hollow core anti-resonant photonic crystal fiber," Opt. Express **29**, 15664–15677 (2021).
25. S. Jiang, P. Yang, Z. Wang, Y. Zhang, W. Bao, and B. Peng, "Dual-parameter sensor for temperature and strain measurement based on antiresonance effect and few-mode fiber," Photonics **10**, 10060642 (2023).
26. S. Liu, T. Yang, L. Zhang, M. Tian, and Y. Dong, "An intensity demodulated refractive index sensor based on a hollow-core anti-resonant fiber," J. Phys. D **55**, 155107 (2022).
27. W. Liu, Y. Shi, Z. Yi, C. Liu, F. Wang, X. Li, J. Lv, L. Yang, and P. K. Chu, "Surface plasmon resonance chemical sensor composed of a microstructured optical fiber for the detection of an ultra-wide

refractive index range and gas-liquid pollutants," Opt. Express **29**, 40734–40747 (2021).
28. W. Liu, C. Liu, J. Wang, J. Lv, Y. Lv, L. Yang, N. An, Z. Yi, Q. Liu, C. Hu, and P. K. Chu, "An intensity demodulated refractive index sensor based on a hollow-core anti-resonant fiber," Results Phys. **47**, 106365 (2023).
29. Q. Liu, J. Sun, Y. Sun, Z. Ren, C. Liu, J. Lv, F. Wang, L. Wang, W. Liu, T. Sun, and P. K. Chu, "Surface plasmon resonance sensor based on photonic crystal fiber with indium tin oxide film," Opt. Mater. **102**, 109800 (2020).
30. Q. Liu, Y. Jiang, Y. Sun, C. Hu, J. Sun, C. Liu, J. Lv, J. Zhao, Z. Yi, and P. K. Chu, "Surface plasmon resonance sensor based on U-shaped photonic quasi-crystal fiber," Appl. Opt. **60**, 1761–1766 (2021).
31. F. Meng, B. Liu, Y. Li, C. Wang, and M. Hu, "Low loss hollow-core antiresonant fiber with nested elliptical cladding elements," IEEE Photonics J. **9**, 7100211 (2017).
32. C. Wei, C. R. Menyuk, and J. Hu, "Geometry of chalcogenide negative curvature fibers for CO_2 laser transmission," Fibers **6**, 74 (2018).
33. C. Wei, J. Hu, and C. R. Menyuk, "Comparison of loss in silica and chalcogenide negative curvature fibers as the wavelength varies," Front. Phys. **4**, 00030 (2016).
34. S. Yan, S. Lou, W. Zhang, and Z. Lian, "Single-polarization single-mode double-ring hollow-core anti-resonant fiber," Opt. Express **26**, 31160–31171 (2018).
35. K. Hu, S. Lou, H. Jia, and X. Wang, "Hybrid structure polarization-maintaining hollow-core photonic bandgap fiber with anti-resonant tubes and silicon layers," Opt. Express **30**, 42035–42045 (2022).
36. D. Yan and J. Li, "Design and analysis of the influence of cladding tubes on novel THz waveguide," Optik **180**, 824–831 (2019).
37. D. Yan and J. Li, "Effect of tube wall thickness on the confinement loss, power fraction and bandwidth of terahertz negative curvature fibers," Optik **178**, 717–722 (2019).
38. M. Meng, D. Yan, Z. Yuan, Q. Feng, X. Li, G. Qiu, J. Li, and J. Li, "Novel double negative curvature elliptical aperture core fiber for terahertz wave transmission," J. Phys. D **54**, 235102 (2021).